Materials Advances

ROYAL SOCIETY OF CHEMISTRY

PAPER

View Article Online
View Journal | View Issue

Cite this: *Mater. Adv.*, 2026, 7, 4670

Tuning the thicknesses, density of states, and electron affinities of the layers in perovskite-based solar cells for green energy solutions

Qayyum ul Hassan, Syed Aqib Abbas Shah, Muhammad Umar Salman, Muhammad Luqman, Muhammad Mehak, Muhammad Javaid Iqbal and Shahid Atiq *

Received 10th January 2026,
Accepted 9th March 2026

DOI: 10.1039/d6ma00053c

rsc.li/materials-advances

The global demand for energy has increased rapidly, highlighting the urgent need for sustainable and renewable energy solutions. Among renewable sources, solar energy has attracted significant attention, with perovskite solar cells (PSCs) emerging as a promising technology. In this context, $BiFeO_3$ (BFO) has gained interest as an absorber material due to its robust remanent polarization and room-temperature ferroelectricity, which eliminates the need for a traditional p–n junction. This study investigates a 3D ZnO/BFO/spiro-OMeTAD PSC architecture using COMSOL Multiphysics simulations. Device performance is influenced by the electron affinity (EA) and density of states (DOS) in BFO, with efficiency varying from 8.96% to 11.28% as these parameters change. Optimization of the photovoltaic parameters yields a maximum efficiency of ~11.83%, a short-circuit current density of ~10.12 mA cm^{-2}, an open-circuit voltage of ~1.8 V, and a fill factor of ~64.91%. The presented simulation framework provides reproducible insights into material and interface optimization, bridging numerical modeling with experimental trends. These findings offer practical guidance for designing high-performance PSCs and advancing next-generation photovoltaic devices.

1. Introduction

Renewable energy is being recognized as a top priority due to the world's growing energy needs (which have increased over the past year by 1.7%) and the pressing need to reduce the release of CO_2 (53.0 Gt) from traditional resources like coal and gasoline.[1–3] In order to meet this rising energy demand, solar power could act as a suitable resource alongside various renewable energy sources, and innovations regarding photovoltaic (PV) technologies have been greatly accelerated by the growing need for energy from renewable sources.[4,5] The development of non-traditional photovoltaic techniques, such as lead-halide perovskite (LHPs), kieserite's, organic material photovoltaics, and oxide-driven solar cells (SCs), has received a lot of attention over the past decade. The investigation of environmentally harmless lead-free (Pb-free) absorber materials has been spurred by worries about toxicity as well as longevity, even though LHPs have shown impressive efficiency.[6] In this regard, oxide- and ferroelectric-derived SCs have become attractive options because of their environmentally friendly nature, chemical stabilization, and stability for scalable manufacturing processes.[7]

Probably the most promising of these developments, perovskite solar cells (PSCs), stand out because of their ferroelectric characteristics, significant dielectric constant (~3.1 to ~7.1), low bonding excitation energy, and large absorption coefficient (10^4–10^5 cm^{-1} at about 400 nm).[8–11] These distinctive characteristics provide perovskite materials with the potential for commercialization and feasible manufacturing in large quantities, allowing them to produce remarkable PV performance.[12] With the goal of achieving the best possible device efficiency along with stability, recent developments in PSCs have highlighted the key impact that material choice plays in the electron transport layer (ETL), PVK absorption layer, and hole transport layer (HTL). Therefore, material tuning has emerged as a robust and rapidly emerging field of study.[13]

In addition to the ETL materials, zinc oxide (ZnO) is a great ETL option because it is a semiconductor having a wide bandgap of ~3.2 eV (at ambient temperature), high affinity for electrons, and an exciton binding energy of 60 meV.[14] Because of its great transparency and elevated electron mobility, which may help in electron transport and lessen unwanted recombination losses, ZnO stands out among the most promising ETL options.[15] In the PVK absorber layer, $BiFeO_3$ (BFO) has become a very attractive material for PV applications because of its unique combination of ferroelectric and antiferromagnetic

Centre of Excellence in Solid State Physics, University of the Punjab, Lahore-54590, Pakistan. E-mail: satiq.cssp@pu.edu.pk

characteristics.[16,17] BFO has garnered significant interest among Pb-free oxide absorbers because of its large absorption coefficient ($\sim 1.88 \times 10^5$ cm^{-1}), low optical band-gap ($E_g \sim 2.5$ eV), and inherent ferroelectric polarization (up to 100 μC cm^{-2}) that can provide effective separation of charges beyond traditional p–n junction methods.[18,19] BFO provides improved photogeneration while maintaining superior thermal and chemical stability, compared to numerous wide E_g oxide materials that have inadequate absorption within the visible spectrum.[20] BFO has shown efficiencies of up to 11.83%, whereas other ferroelectric materials have shown efficiencies of about 0.1%.[21] With a rhombohedral shape, BFO also has high Curie and Néel temperatures of around 1103 K and 643 K, respectively.[22] Numerous investigations show that BFO is a p-type material since its Fermi level lies close to its valence band.[23] The HTL has become equally critical since it controls effective hole collection and transport. Spiro-OMeTAD, a popular HTL material, exhibits outstanding performance because of its exceptional hole mobility, superior thin film formation, and stable operation, and because of its coherence with BFO, recombination losses are decreased and charge transport ability is increased.[24–27] In contrast to previous oxide and chalcogenide absorbing material designs, 3D ZnO/BFO/spiro-OMeTAD coupling thus serves as a dynamically balanced configuration that combines stability, Pb-free architecture, and ferroelectric-aided carrier kinetics.

Making use of these traits, Wani *et al.* (2024) claimed that the short-circuit current density (J_{sc}), V_{oc}, fill factor (FF), and efficiency outcomes for the ITO/ZnO-uc/BFO/AI architecture were found to be 4.7 mA cm^{-2}, 0.89 V, 53%, and 2.21%, respectively.[28] Likewise, Afzal *et al.* (2020) investigated the ITO/graphene/ZnO/BFO/graphene design, achieving an efficiency of 7.8% along with $V_{oc} \sim 0.6$ V and $J_{sc} \sim 13.155$ mA cm^{-2}.[29] Similarly, Raj *et al.* (2024) reported that the FTO/ZnO/BFO/spiro-OMeTAD/Au solar cell exhibited a $V_{oc} \sim 0.79$ V, $J_{sc} \sim 8.35$ mA cm^{-2}, FF $\sim$ 29.10%, and efficiency of 1.92%.[30] Furthermore, innovation was shown by Mahammedi *et al.* (2024), who tuned the bandgap (E_g) of Bi_2FeCrO_6 between 1.4 eV and 2.4 eV using Fe/Cr cationic ordering, reaching an efficiency of 7.3% with FF $\sim$ 53.7%, $J_{sc} \sim 12.15$ mA cm^{-2}, and $V_{oc} \sim 1.12$ V.[31]

Given these encouraging characteristics, the photovoltaic potential of 3D ZnO/BFO/spiro-OMeTAD PSCs is still constrained by a lack of knowledge regarding active layer thickness tuning, interfacial band alignment, and the impact of DOS upon the transport of carriers, particularly recombination. In this research, a comprehensive numerical study of 3D ZnO/BFO/spiro-OMeTAD SCs is performed, with an emphasis on the combined impacts of DOS engineering, EA adjustment, and absorber layer thickness on performance. In contrast to earlier research that mostly reports isolated parameter alterations or experimental efficiency, this work offers a cohesive and physically oriented analysis connecting material attributes to photovoltaic parameters. Hence, these findings provide predictive design guidance to support experimental attempts to optimize Pb-free BFO-based PSCs. In this study, the 3D ZnO/BFO/spiro-OMeTAD framework is totally toxic-free, thermally resistant, and readily accessible and an investigation is conducted to comprehend the parameters that currently limit its performance.

2. Theoretical framework

The 3D ZnO/BFO/spiro-OMeTAD solar cells (SCs) operate as a multi-layered system, meticulously designed for optimal photon capture and efficient charge transport. Here, ZnO works as the electron transport layer (ETL), BFO takes on the role of the primary photon-absorbing material, and spiro-OMeTAD serves as the dedicated conduit for hole transport. The theoretical framework intertwines optical dynamics, charge kinetics, interfacial phenomena, and material-specific parameters of the absorber layer, including EA, DOS, thickness, and Fermi–Dirac principles. Therefore, three fundamentally important differential equations, the Poisson's equation (eqn (1)), the continuity principle (eqn (2)), and the transport principle (eqn (3)), form the basis of the simulation, enabling an in-depth investigation of the function of solar cells. In photovoltaic cells, the carrier's dynamics is controlled by transport formulas. In contrast, Poisson's equation describes how charges are distributed along the electric field, and the continuity expression deals with recombination as well as carrier production.

$$\frac{\partial^2 \varphi}{\partial^2 x} = -\frac{\partial E}{\partial x} = -\frac{q}{\varepsilon_s}[p - n + N_D(x) - N_A(x) \pm N_{def}(x)] \quad (1)$$

$$\frac{\partial n,p}{\partial t} = \frac{1}{q}\frac{\partial J_n}{\partial x} + (G_n - R_n) + \frac{1}{q}\frac{\partial J_p}{\partial x} + (G_p - R_p) \quad (2)$$

$$J_{n,p} = nq\mu_n E + qD_n\frac{\partial n}{\partial x} + nq\mu_p E + qD_p\frac{\partial p}{\partial x} \quad (3)$$

Here, in eqn (1)–(3), φ symbolizes the electrostatic potential, ε_s is the permittivity of the material, n and p are the free electron/hole densities, N_D and N_A are donor and acceptor impurities, N_{def} is the defect density, electron/hole current density is represented by $J_{n,p}$, q is the charge, and μ_{np} is the charge dynamics. The aforementioned mathematical equations were successfully solved regarding steady-state settings using the semiconductors module of COMSOL Multiphysics. The conducting electrodes were made to satisfy boundary conditions that corresponded to ohmic, especially selective, connections. All of these equations directly affect the computed current–voltage properties, such as band bending, and in addition the inner electric fields are governed by the Poisson's equation, the carrier's harvesting under illumination was computed by the continuity mathematical models, and non-radiative impacts are controlled by the corresponding DOS recombination factors. Therefore, the quantitative assessment of the material factor's effects on quantifiable photovoltaic outcomes is made possible by this coupled approach.[32–36]

The recombination processes play a key role in determining how efficient a device is, and radiative recombination occurs by photon emission, whereas Shockley–Read–Hall (SRH)

recombination takes into account trap states inside the E_g. The continuity models are modified to include such recombination mechanisms for the purpose of accounting for the dynamics underlying carrier loss. The SRH recombination process reveals the pathway through which charge carriers annihilate *via* intermediary defect states or traps embedded in a semiconductor's E_g. These impurity or structural anomaly-induced traps serve to impede the carrier dynamics. The SRH recombination has a significant impact on semiconductor device performance, particularly when defect-driven mechanisms take center stage or the pristine substance is simply not available.[37] The SRH recombination and the carrier lifetimes are calculated from eqn (4) and (5).[38]

$$R_{\mathrm{RSH}} = \frac{np - n_i p_i}{\tau_n(p + p_1) + \tau_{p(n+n_1)}} \tag{4}$$

$$\tau_{n,p} = \frac{1}{N_t V_{\mathrm{th}} \sigma_{n,p}} \tag{5}$$

Here, in eqn (4) and (5), N_t shows the defect density, V_{th} denotes the thermal velocities of electrons and holes (e/h), $\sigma_{n,p}$ symbolizes the capture cross-sectional areas of electrons and holes, and $\tau_{n,p}$ represents the carrier lifetimes of electrons and holes. The FF controls how a SC behaves overall, whereas efficiency is defined as simply the relation regarding its output power and input power. The FF ranges from 0 to 1, with a closer value to 1 indicating improved SC performance.[39,40] The values of these two quantities can be acquired from the following relations (eqn (6) and (7)).

$$\mathrm{FF} = \frac{J_{\max} \times V_{\max}}{J_{\mathrm{sc}} \times V_{\mathrm{oc}}} \tag{6}$$

$$\mathrm{PCE} = \frac{V_{\mathrm{oc}} \times J_{\mathrm{sc}} \times \mathrm{FF}}{P_{\mathrm{in}}} \tag{7}$$

Overall, the computational procedure used in this investigation is summed into a format that guarantees reproducibility of the final outcomes given. Initially, device design along with the thickness of the layers was determined using studies on BFO-related heterojunctions that have been published. Under AM1.5G light, photo generation was computed utilizing BFO's wavelength-based absorption characteristic. In order to simulate carrier transport, Poisson's differential equation was systematically solved and coupled with the e/h continuity principle, adding SRH recombination according to distributed DOS and additionally drift diffusion transportation. Additionally, a distinct correlation connecting a specific physical mechanism as well as device operational parameters was made possible by methodically varying each material property one at each step while maintaining the same values for every other. Table 1 provides the layer-specific optimized parameters, sourced individually from the relevant studies, with simulations conducted at a temperature of 293 K.

Table 1 Basic input optimized parameters of each layer in the 3D ZnO/BFO/spiro-OMeTAD PSC

Material properties	ZnO	BFO	Spiro-OMeTAD
Relative permittivity	6	6	3
Band gap (eV)	3.2	2.5	3
Electron affinity (eV)	3.8	2.8	1.9
Effective DOS valence band (cm^{-3})	1×10^{20}	5×10^{18}	1×10^{20}
Effective DOS conduction band (cm^{-3})	1×10^{20}	5×10^{18}	1×10^{20}
Electron mobility ($cm^2\ V^{-1}\ s^{-1}$)	150	80	2
Hole mobility ($cm^2\ V^{-1}\ s^{-1}$)	25	25	1×10^{-2}
Electron lifetime, SRH (ns)	1	1000	1
Hole lifetime, SRH (ns)	1	1000	1

3. Results and discussion

3.1 Energy level schematic diagram

Fig. 1(a) depicts a 3D ZnO/BFO/spiro-OMeTAD SC with ZnO acting as the ETL, BFO being the incident photon absorbing perovskite, and spiro-OMeTAD gathering holes for effective separation of charges and transportation. Fig. 1(b) shows that the BFO layer absorbs photons to create electron–hole pairs, which are then transmitted to the ETL and gather at its front contact. In contrast, holes are moved to the rear contact *via* the HTL, and this process demonstrates energy-level proper alignment as well as transportation of charges in the SCs. Here, crossed arrows guarantee selective charge transfer and lower recombination losses by indicating electrons that are unable to approach the HTL, as well as holes that are kept from doing so. Fig. 1(c) illustrates the optical staggered band configuration that guarantees efficient charge carrier segregation as well as transport across the optical energy band structure of 3D ZnO/BFO/spiro-OMeTAD SCs. Its quasi-Fermi states regarding electrons (E_{fn}) as well as holes (E_{fp}) show the mobility of the charges. In contrast, the conduction band edge (E_c) and also the valence band edge (E_v) show the alignment throughout its layer structure. Staggered alignment minimizes recombination, as well as carrier backflow, and maximizes performance as electrons flow towards the ETL while holes are guided towards the HTL.[41]

3.2 Solar irradiance and generation rate

Fig. 2(a) reveals the solar irradiance at different wavelengths assuming as the light source, A.M 1.5 G, within the visible region (400–700 nm), attaining a luminosity peak of $\sim$1.6 W m^{-2} nm^{-1} at around 460 nm, indicating the efficient availability of visible light to generate charge carriers. Irradiance decreases after 1000 nm, indicating insignificant solar energy over the infrared spectrum. Fig. 2(b) shows in what way the extinction coefficient (k) as well as the refractive index (n) change with wavelength; the n value is larger in the UV region while it steadily decreases for both the visible and IR zones. This suggests improved light trapping and decreased reflection, especially in the UV-visible range. On the other hand, because of strong electronic transitions, k is high for the UV, decreases during the visible region and is minimal for the IR, which remains consistent with the cell's absorbing properties. Fig. 2(c) illustrates that light

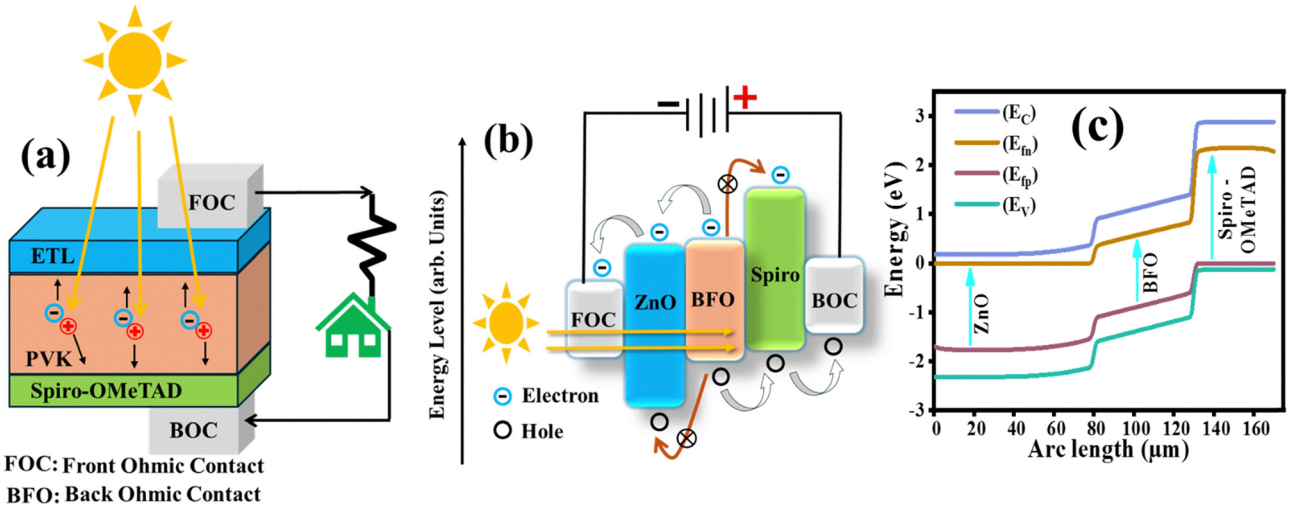

Fig. 1 (a) Solar cell schematic diagram of the ZnO/BFO/spiro-OMeTAD architecture, (b) schematic with arbitrary energy levels to show the available paths for electrons and holes, and (c) energy band diagram under illumination as a function of arc length.

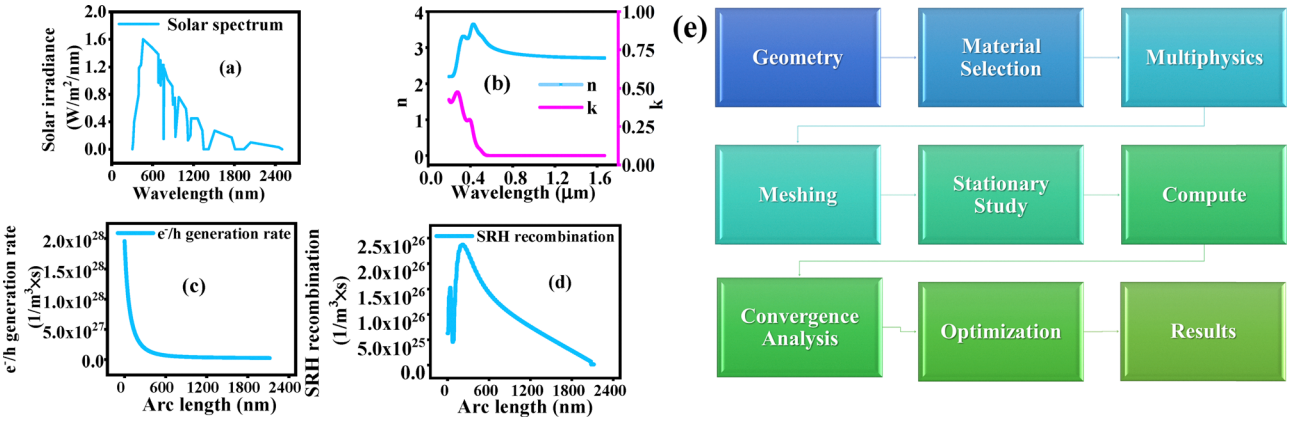

Fig. 2 (a) Solar spectrum AM 1.5G, (b) variation of refractive index and extinction coefficient (*n*,*k*) with respect to wavelength, (c) electron/hole generation rate as a function of arc length, (d) Shockley–Read–Hall (SRH) recombination as a function of arc length, and (e) schematic flowchart, highlighting the essential steps for device building.

absorption falloffs deeper within the absorber layer, and the electron/hole (e/h) pair creation rate drops exponentially on increasing arc length, consistent with the law of Beer–Lambert. Fig. 2(d) shows that due to the lower concentration of carriers close to the surface, the SRH recombination pattern starts at a lower arc length and a minor increase in recombination occurs by increasing the carrier concentration as the arc length increases. Following this, as carriers start to diffuse farther within the absorber layer, lowering localized recombination, this rate momentarily decreases.[42]

3.3 Device construction layout

The 3D ZnO/BFO/spiro-OMeTAD PSCs were simulated in COMSOL Multiphysics, and the process begins with specifying the actual geometry, in which ZnO (ETL), BFO (PVK), and spiro (HTL) layers are precisely denoted in the 3D device layout and layer's set-up. The next step is material choice, where each individual layer is given the optimal electrical along with optical characteristics. After that, for the sake of simultaneous results, a multiphysics component is chosen to group the semiconductor with optical physical phenomena. Subsequently, the linked governing formulas were processed numerically right through the computing phase, and in addition steady-state computations under illumination along with bias settings were obtained by stationary investigation. Soon after that, the domain was discretized *via* meshing, with improved elements at key contacts to achieve numerical correctness. Moreover, convergence analysis works out to verify mesh validity and solution consistency, confirming the accuracy of its results. Later, the model undergoes optimization with key factors like thickness of the layers or DOS being methodically changed to improve device function. Eventually, the optimal data are obtained as photovoltaic performance measurements, especially *J*–*V* characteristics of the device. Fig. 2(e) demonstrates the schematic diagram and provides procedural guidance for

using the COMSOL Multiphysics program to replicate this structure.

The optical input for the simulation is the standard AM 1.5 solar spectrum, which is used as the illumination source to evaluate realistic photovoltaic operation under one-sun conditions. At the material level, all layer specific parameters including band gap, electron affinity, relative permittivity, carrier mobilities, effective density of states, and recombination parameters are taken as direct inputs, as summarized in Table 1. These parameters define the physical behavior of each functional layer in the device stack and form the basis of the numerical model.

Several physical and numerical assumptions are adopted to make the problem well defined and computationally stable. The device is assumed to be directly exposed to the environment, meaning encapsulation or a top glass layer is considered, so optical losses due to external shielding are neglected. All interfaces are assumed to be homogeneous, with abrupt and ideal transitions between adjacent layers, without interfacial roughness or compositional grading. Carrier transport is modeled by solving the coupled Poisson and continuity equations for both electrons and holes. Fermi–Dirac statistics are employed instead of Maxwell–Boltzmann statics to obtain more accurate carrier distributions, particularly under high doping and strong electric field conditions. The interface continuation parameter is assumed to be ideal and set equal to unity, implying perfect electrical continuity across interfaces. No coupling between doping profiles and trap states is assumed and trap-assisted tunneling is neglected. Tunneling mechanisms are therefore disabled in the model. For numerical discretization, a finite volume approach is adopted with constant shape functions, ensuring charge conservation and numerical robustness. In heterojunction regions, quasi-Fermi levels are assumed to describe carrier transport under non-equilibrium conditions. Finally, the metal contacts are modeled as pure ohmic contacts, neglecting contact resistance and Schottky barrier effects, in order to focus on intrinsic device physics.

3.4 Effect of BFO's thickness variation on PV performance

The absorbing layer as well as its thickness in the solar cell plays a pivotal role in output performance. Fig. 3(a) shows a schematic illustration of the effect of the absorbing layer and its thickness, showing that photo-generated carriers are created, separated, and transported, and elevated thickness causes recombination (R_{ETL}, R_{HTL}), that lowers efficiency. Fig. 3(b) and (c) illustrate improved light absorption as well as effective charge transfer in 3D ZnO/BFO/spiro-OMeTAD SCs, and provide the *J*–*V* and *P*–*V* characteristics. Power output drops as BFO's thickness increases, it peaks at 108.14 W (300 nm) and then gradually drops towards 40.24 W (1550 nm) as a result of recombination losses. Fig. 3(d) depicts variation in J_{sc}, V_{oc}, and P_{max}: here J_{sc} rises from 9.92 mA cm^{-2} (at 300 nm) as the thickness of the active layer increases, reaching its highest value of ~10.35 mA cm^{-2} (at 800 nm). Beyond this point, it levels off at approximately ~10.32 mA cm^{-2} within the range of 1050–1300 nm, before eventually falling to 9.30 mA cm^{-2} at 1550 nm, signifying the optimal thickness for achieving maximum J_{sc}. It also indicates that enhanced photon absorption along with energy alignment cause V_{oc} to increase from 1.7 V (at 300 nm) to 1.8 V (at 550 nm–800 nm). However, after 800 nm, V_{oc} marginally drops and stabilizes at around 1.7 V for thicknesses reaching 1550 nm, suggesting that the saturation effect predominates at greater thicknesses. Yet, P_{max} stays relatively stable between 108.1 W and 104.7 W for thicknesses between 300 and 800 nm, then gradually decreases to 98.8 W (at 1300 nm) due to reduced charge

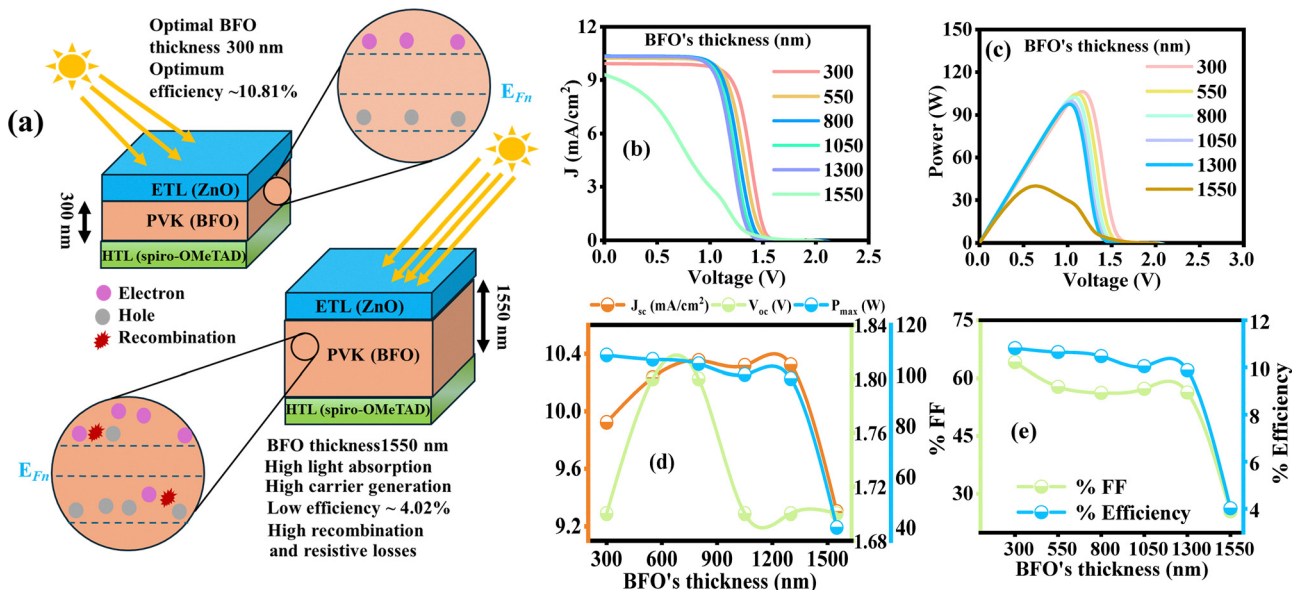

Fig. 3 (a) Schematic illustration of the solar cell working, highlighting the effect of BFO's thickness variation on (b) the *J*–*V* curve, (c) the *P*–*V* curve of the 3D ZnO/BFO/spiro-OMeTAD solar cell and the effect of BFO's thickness variation on (d) J_{sc}, V_{oc}, and P_{max}, and (e) %FF, and %efficiency with respect to BFO's thickness variation.

Table 2 Designed structure (3D ZnO/BFO/spiro-OMeTAD) output performance parameters with varying BFO thickness

BFO thickness (nm)	J_{sc} (mA cm^{-2})	V_{oc} (V)	P_{max} (W)	FF%	Efficiency%
300	9.92	1.7	108.14	64.11	10.81
550	10.23	1.8	106.46	57.79	10.65
800	10.35	1.8	104.73	56.20	10.47
1050	10.32	1.7	100.47	57.28	10.05
1300	10.32	1.7	98.82	56.31	9.88
1550	9.30	1.7	40.24	25.45	4.02

collection effectiveness. P_{max} sharply decreases to 40.2 W (at 1550 nm), most likely caused by optical loss outweighing the benefits of increased thicknesses. Fig. 3(e) shows %FF and %efficiency behavior, which reflects that when the resistive effect increases, the FF decreases from 64.11% (at 300 nm) to the range of 56.20–57.28% for (1050–1300 nm), suggesting a stable but decreasing performance. The sharp decline in FF to 25.4% (at 1550 nm) is probably caused by substantial recombination and ineffective carrier transportation. This shows steady performance with minimal efficiency losses resulting from increased thickness, beginning at 10.81% (at 300 nm) and decreasing to 9.88% (at 1300 nm). At 1550 nm, on the other hand, the efficiency declines precipitously to 4.02%, most likely as a result of reduced carrier transport efficiency along with significant optical losses.[43] Table 2 provides the effect of BFO's thickness variation on the output characteristics of the photovoltaic performance of the proposed SC configuration.

3.5 Effect of ZnO's thickness variation on PV performance

Fig. 4(a) lays out the study associated with ZnO's thickness, showing an ideal thickness of 40 nm at which J_{sc} ($\sim$8.83 mA cm^{-2}) is maximum. As thickness increases (10–40 nm), V_{oc} steadily increases from 2.02 to 2.03 V and reaches an optimum value of $\sim$2.23 V (at 50 nm); hence, after this ideal thickness (50 nm), V_{oc} starts decreasing slowly to $\sim$2.03 V (at 60 nm). This may be due to insufficient light absorption as well as high series resistance (R_S) inside the device architecture. Fig. 4(b) shows that the power output measurement for different ZnO thicknesses reveals a gradual increase from 117.85 W (at 10 nm) to 118.12 W (at 60 nm), as thinner layers (10–50 nm) harvest relative lower power output. This is due to the lower charge transfer and poor light harvesting effect, and a gradual increase in thickness above 50 nm improves light absorption, which ultimately enhances power output. Fig. 4(c) exhibits the J_{sc}, V_{oc}, and P_{max}, in which J_{sc} starts rising from 8.82 mA cm^{-2} (at 10 nm) until a maximum of 8.83 mA cm^{-2} (at 40 nm) and remains steady towards 60 nm as a result of excellent light absorption, and charge collecting ability. Furthermore, V_{oc} increases as ZnO's thickness increases; it starts from 2.02 V (at 10 nm), and attains a maximum of 2.23 V (at 50 nm), and then drops gradually to 2.03 V after the ideal thickness of 50 nm. The main cause of this behavior is the increase in R_S and reduction in electric field, each of which makes it more difficult for charges to separate and move through the device effectively. But P_{max} increases as ZnO's thickness increases, reaching the maximum power peak of $\sim$118.12 W at 60 nm, which is due to the higher light absorption, optimum transport of charges, and low resistance. Fig. 4(d) illustrates the %FF and %efficiency trend; FF gets improved as ZnO's thickness increases (10–30 nm) due to improved charge extraction, yet it gets a little lower after 30 nm because of the increase in resistance. On the contrary, as ZnO's thickness increases, the efficiency rises from $\sim$11.78% (at 10 nm) to $\sim$11.82% (at 60 nm) because of the increase in absorption, charge transport strength, and reduced R_S; therefore the thicker ZnO layer (60 nm) yields the optimum efficiency.[44] Table 3 provides the effect of ZnO's thickness variation on the output characteristics of the PV performance of the proposed SC configuration.

3.6 Effect of BFO's DOS variations on PV performance

Fig. 5(a) illustrates the dynamics variation in the DOS within the BFO layer of the 3D ZnO/BFO/spiro-OMeTAD PSC and provides the *J–V* characteristics. However, a fascinating interplay emerges in the V_{oc}, which exhibits a significant decline as DOS escalates at $N_{c/v} = 1 \times 10^{16}$ cm^{-3}. The V_{oc} reaches an optimal magnitude of 1.8 V, and after this it gradually decreases to 1.5 V at 1×10^{20} cm^{-3}. This compelling behavior highlights the profound impact of increased DOS, which intensifies recombination losses, slightly decreasing V_{oc} whereas J_{sc} persistently holds its ground. Fig. 5(b) shows that with rising DOS, the power output declines from $\sim$118.28 W to $\sim$89.93 W, as V_{oc} reduces from 1.8 V to 1.5 V, owing to amplified recombination and resistive losses obstructing carrier transportation. Fig. 5(c) shows the variation in J_{sc}, V_{oc}, and P_{max}, which reveals the constancy of J_{sc} ($\sim$10.123 mA cm^{-2}) within the DOS span of 1×10^{16}–1×10^{19} cm^{-3}, suggesting that photonic generation and carrier extraction are mainly tolerant to DOS fluctuations in this domain. Because of increased carrier recombination being linked to higher DOS, the V_{oc} gradually drops. As a result of higher non-radiative expenses and shorter carrier lifetime, the P_{max} and FF decrease. However, a slight rise in J_{sc} ($\sim$10.124 mA cm^{-2}) at 1×10^{20} cm^{-3} corresponds to computing tolerance and is not indicative of some sort of fundamental transport change, but rather a small shift towards the band-edge carrier density. Consequently, this demonstrates that DOS modifications mostly affect the quasi-Fermi level splitting along with the recombination dynamics, instead of the J_{sc} generation process. However, V_{oc} drops primarily because of the enhanced non-radiative recombination caused by an increase in DOS, leading to greater energy dissipation, and limiting the achievable voltage. This effect is commonly observed in PSCs in which a large number of states trap charge carriers, reducing the separation of quasi-Fermi levels. This further indicates that as DOS rises from 1×10^{16}–1×10^{20} cm^{-3}, P_{max} falls suggesting that higher DOS results in increased recombination and lower power generation. Fig. 5(d) shows the variation in %FF and %efficiency; FF marginally rises at 1×10^{17} cm^{-3} because of better carrier transport, yet it falls after that due to higher DOS, which leads to more non-radiative recombination that impairs productivity. Correspondingly, efficiency falls from $\sim$11.83% (at 1×10^{16} cm^{-3}) to 8.99% at 1×10^{20} cm^{-3} and this is due to the effect that the increase in

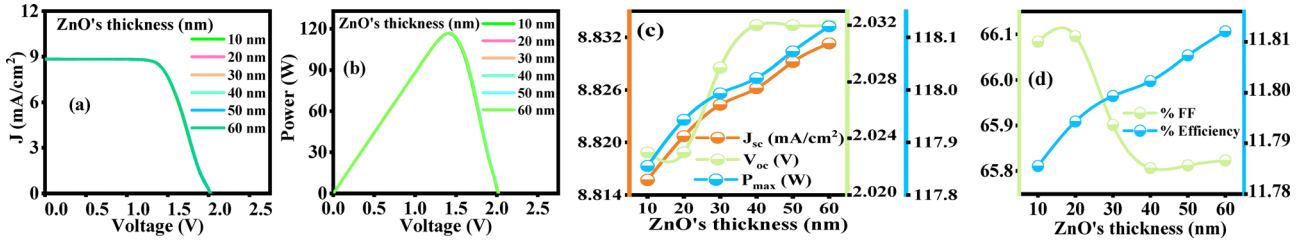

Fig. 4 (a) J–V curves and (b) P–V curves for varied ZnO thicknesses in the 3D ZnO/BFO/spiro-OMeTAD solar cell and their effects on (c) J_{sc}, V_{oc}, and P_{max}, and (d) %FF, and %efficiency.

Table 3 Designed architecture (3D ZnO/BFO/spiro-OMeTAD) performance parameters with varying ZnO thickness

ZnO thickness (nm)	J_{sc} (mA cm^{-2})	V_{oc} (V)	P_{max} (W)	FF%	Efficiency%
10	8.82	2.02	117.85	66.08	11.785
20	8.82	2.02	117.94	66.10	11.794
30	8.82	2.03	117.99	65.90	11.799
40	8.83	2.03	118.02	65.81	11.802
50	8.83	2.23	118.07	65.81	11.807
60	8.83	2.03	118.12	65.82	11.812

Table 4 Designed architecture (3D ZnO/BFO/spiro-OMeTAD) performance parameters with varying density of states (DOS) in the conduction and valence band (N_c, N_v) of the BFO layer

N_c and N_v (cm^{-3})	J_{sc} (mA cm^{-2})	V_{oc} (V)	P_{max} (W)	FF%	Efficiency%
1×10^{16}	10.123	1.8	118.28	64.91	11.83
1×10^{17}	10.123	1.7	113.30	65.83	11.33
1×10^{18}	10.123	1.6	106.15	65.54	10.62
1×10^{19}	10.123	1.6	100.88	62.28	10.09
1×10^{20}	10.124	1.5	89.93	59.22	8.99

DOS provides more trapping states, which ultimately speeds up recombination, and shortens the carrier lifetime.[45] Table 4 provides the output characteristics of the proposed SC configuration at varying DOS of the BFO layer.

3.7 Effect of electron affinity (EA) of the absorbing layer on PV performance

Electron affinity is a key parameter governing energy band alignment at the interfaces between the absorber and charge transport layers in photovoltaic devices. Proper electron affinity alignment controls the conduction and valence band offsets, enabling efficient electron extraction to the electron transport layer and hole transport layer. Favorable band offsets reduce interfacial energy barriers and suppress carrier recombination losses. As a result, charge separation and transport are enhanced, leading to improved short-circuit current density and open-circuit voltage. Consequently, optimized electron affinity contributes directly to the higher overall power conversion efficiency.

Fig. 6(a) illustrates the J–V curve, and Fig. 6(b) shows the P–V characteristics at different electron affinities of the absorbing layer. The P_{max} value increased with the BFO electron affinity due to maximum generation of charge carriers like electrons and holes and lower recombination. Fig. 6(c) shows the variation in J_{sc}, V_{oc}, and P_{max} at the same range of electron affinities, where a slight change in J_{sc} happens as EA decreases, and beyond the point at 2.5 eV it stabilized at 8.82 mA cm^{-2} for greater EA (2.6–2.8 eV) due to maximum recombination occurring of charge carriers and some other factors like increased defects. On the other hand, V_{oc} is maximum (2.39 V) at 2.5 eV because of optimized energy alignment and then decreases to the minimum value of 2.03 V at 2.6–2.8 eV, possibly as a result of increased E_c offset. It also shows that P_{max} gradually rises from ~89.65 W (at 2.5 eV) to a maximum output of ~112.79 W (at 2.8 eV); owing to this, 2.8 eV signifies ideal energy-alignments, lower energy loss during charge extraction, a strong built-in electric field, enhanced electron injection into the ETL, improved conduction band alignment with the ETL and higher generation of charge carriers. Fig. 6(d) exhibits the variation in %FF and %efficiency at different EA values, which illustrates that the FF increases continuously from 42.49% (at 2.5 eV) to a maximum magnitude of 63.01% (at 2.8 eV), suggesting a good balance between the photo generated carriers, and their collection at the respective terminals with

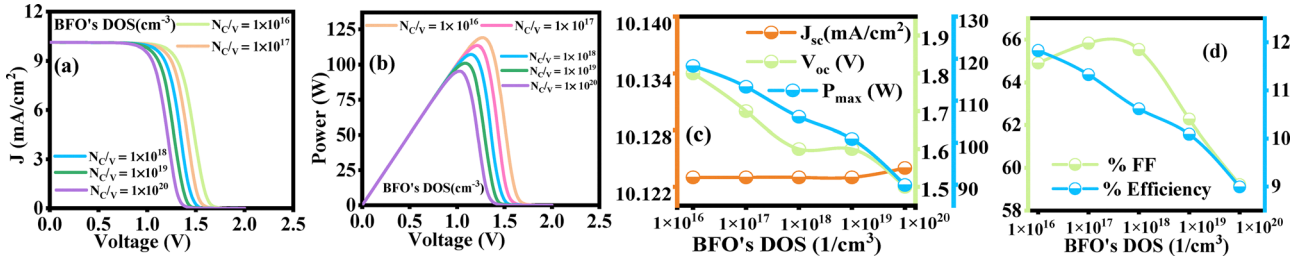

Fig. 5 (a) J–V curves, (b) P–V curves for varied BFO conduction (N_c) and valence band (N_v) density of states (DOS) in the 3D ZnO/BFO/spiro-OMeTAD solar cell and their effects on (c) J_{sc}, V_{oc}, and P_{max}, and (d) %FF, and %efficiency.

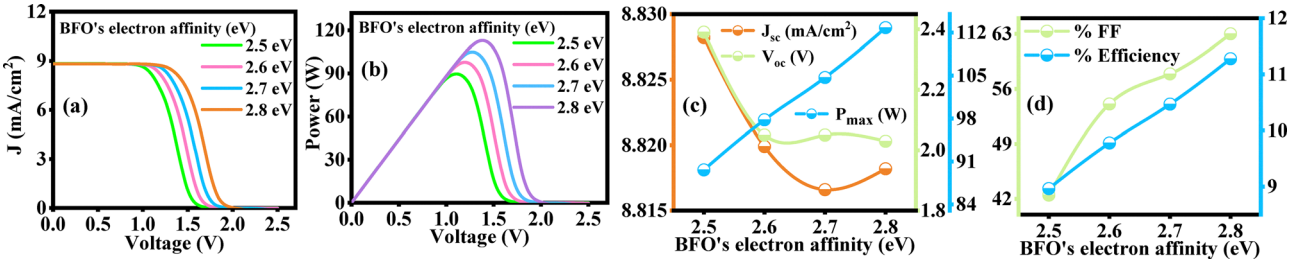

Fig. 6 (a) *J*–*V* curves and (b) *P*–*V* curves for varied BFO electron affinity in a 3D ZnO/BFO/spiro-OMeTAD solar cell and their effects on (c) J_{sc}, V_{oc}, and P_{max}, and (d) %FF, and %efficiency.

increasing EA. Probably, it further demonstrates that the optimum energy-level alignment increases the carrier's transport and reduces recombination, which ultimately causes the efficiency to increase from ~8.96% (at 2.5 eV) to a peak of ~11.28% (at 2.8 eV). Of course, an EA of 2.5 eV yields an optimal V_{oc} of 2.39 V, and a cut down V_{oc} of 2.03 V results in the optimal efficiency at 2.8 eV. This noticeable disparity is caused by the trade-off involving carrier transportation and increased V_{oc}. A higher E_c mismatch within the device's boundaries enhances quasi-Fermi level division as well V_{oc} at lowered EA to suppress interfacial recombination. Nevertheless, this misalignment causes an extraction limitation, which raises resistive losses and thus lowers FF. On the other hand, optimized alignment results from the EA of 2.8 eV, which promotes effective transportation of carriers, better carrier selectivity at the interface, and lower energy loss during charge extraction and a greater FF. Therefore, the increase in FF exceeds the decrease in V_{oc}, leading to a higher total efficiency.[46] Table 5 provides the effect of BFO's EA variation on the output characteristics of PV performance of the proposed SC configuration.

The photovoltaic success of several BFO-based solar cell topologies is summarized in the comparison in Table 6, which shows a noticeable increase in efficiency with interfacial as well as transportation layer engineering improved. As a consequence of the restricted FF and carrier extraction, common FTO/BFO/spiro-OMeTAD/Au modeled design displays poor efficiency (1.98%), highlighting the intrinsic recombination effects.[47] However, the efficiencies significantly rise when better aligned ETL layers are added, such as in ZnSe/BFO/spiro-OMeTAD (10.73%)[48] and ZnO/BFO/GO (11.39%) constructed designs.[49] This enhancement is further increased in multi-layer structures like TiO_2/SnS/BFO/spiro-OMeTAD, in which sequential energy alignment improves the separation of carriers along with light absorption, leading to maximum theoretical efficiency (23.59%).[50] On the other hand, ferroelectric heterostructures such as ITO/i-BFCO/*n*-Nb:STO exhibit relatively low efficiency (0.82%), indicating that transport constraints or suboptimal interfaces can't be compensated just by ferroelectric polarization only.[51] Whereas, concentrating on those experimentally recorded BFO-based structures, the performance behavior clearly demonstrates interfacial DOS along with charge transportation layer characteristics. The graphite/BFO/ZnO/ITO/SLG exhibits the maximum efficiency (3.98%), mainly because of its modest FF (50.4%) and comparatively large J_{sc} (12.47 mA cm^{-2}).[52] Additionally, due to its exceptionally low FF (0.39%) and J_{sc} (1.90 mA cm^{-2}), the NiO/BFTO/WS_2 structure exhibits inadequate efficiency (0.88%) and substantial interfacial losses.[53] Ultimately, the worst performance is seen regarding FTO/BFO/GO, in which ineffective transportation of carriers across the entire GO interface is confirmed by insignificant J_{sc} (0.134 mA cm^{-2}) and efficiency (0.0207%).[54] Furthermore, ITO/ZnO-uc/BFO/AI[27] and AI/BFO/ITO show substantially lower efficiencies, suggesting increased junction selectivity together with reduced carrier extraction and greater

Table 5 Designed structure (3D ZnO/BFO/spiro-OMeTAD) performance parameters with varying electron affinity (EA) of the BFO layer

EA (eV)	J_{sc} (mA cm^{-2})	V_{oc} (V)	P_{max} (W)	FF%	Efficiency%
2.5	8.83	2.39	89.65	42.49	8.96
2.6	8.82	2.05	97.79	54.08	9.78
2.7	8.82	2.05	104.69	57.92	10.47
2.8	8.82	2.03	112.79	63.01	11.28

Table 6 Comparative analysis of the physical parameters of various BFO-based simulation and experimental device structures for efficient solar cell design

Solar cell structure	J_{sc} (mA cm^{-2})	V_{oc} (V)	FF%	Efficiency%	Ref.
FTO/BFO/spiro-OMeTAD/Au (simulation)	8.35	0.79	29.10	1.92	47
ZnSe/BFO/spiro-OMeTAD (simulation)	8.83	1.96	61.91	10.73	48
ZnO/BFO/GO (simulation)	8.93	2.21	71.47	11.39	49
TiO_2/SnS/BFO/spiro-OMeTAD (simulation)	29.83	0.95	82.83	23.59	50
ITO/i-BFCO/*n*-Nb:STO (simulation)	4.0	0.41	49.8	0.82	51
Graphite/BFO/ZnO/ITO/SLG (experimental)	12.47	0.642	50.4	3.98	52
ITO/ZnO-uc/BFO/AI (experimental)	4.7	0.89	53	2.21	28
NiO/BFTO/WS_2 (experimental)	1.90	0.8	0.39	0.88	53
FTO/BFO/GO (experimental)	0.134	0.33	46.87	0.0207	54
AI/BFO/ITO (experimental)	2.34	0.92	37	0.89	55
3D ZnO/BFO/spiro-OMeTAD	10.12	1.8	64.91	11.83	This work

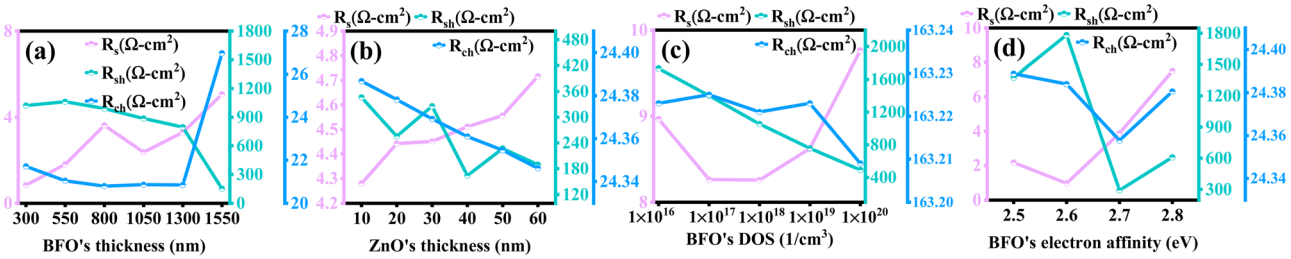

Fig. 7 Variation of series resistance (R_s), shunt resistance (R_{sh}), and characteristic resistance (R_{ch}) with respect to (a) BFO's layer thickness, (b) ZnO's layer thickness, (c) the DOS of the BFO layer, and (d) BFO's electron affinity.

recombination near metal contacts.[55] In the aforementioned settings, our suggested 3D ZnO/BFO/spiro-OMeTAD configuration provides superior FF (64.91%) along with significant V_{oc} (1.8 V) to attain 11.83% efficiency. Consequently, the 3D ZnO/BFO/spiro-OMeTAD architecture improves extrication of carriers along with optical absorption, demonstrating that interfacial settings along with nanostructured ETLs are essential for the advancement of BFO-based solar cells.

3.8 Resistance analysis

Fig. 7(a) illustrates the relationship b/w the series resistance (R_s), shunt resistance (R_{sh}), and characteristic resistance (R_{ch}) as a function of BFO layer thickness, varied from 300 to 1550 nm. The minimum R_s value (0.83 Ω cm^2) is observed at lower BFO thickness, which can be attributed to reduced charge carrier recombination and the relatively low intrinsic resistivity of the BFO layer under optimized conditions. As the BFO thickness increases to 1550 nm, R_s progressively rises to 5.06 Ω cm^2, primarily due to enhanced bulk recombination and the increased density of structural defects associated with thicker films. The R_{sh} reaches a maximum value of 1062 Ω cm^2 at a BFO thickness of 550 nm, indicating minimal leakage pathways and suppressed interfacial recombination. However, further increasing the thickness results in a substantial decrease in R_{sh} to approximately 150 Ω cm^2, which is attributed to the formation of interfacial defects and additional recombination centers that facilitate leakage currents. The overall R_{ch}, representing the combined influence of these resistive components, attains its maximum value (~26.96 Ω cm^2) at a BFO thickness of 1550 nm, reflecting the cumulative effect of increased bulk and interfacial resistive losses.

Fig. 7(b) presents the dependence of R_s, R_{sh}, and R_{ch} on the thickness of ZnO. The minimum R_s value (4.28 Ω cm^2) is observed at lower ZnO thickness, indicating reduced recombination losses and improved crystalline quality. As the ZnO layer thickness increases, R_s gradually increases to a maximum value of ~4.71 Ω cm^2, which may be attributed to enhanced charge carrier recombination and increased structural imperfections. The highest R_{sh} value (~346 Ω cm^2) is obtained at a lower ETL thickness of ~10 nm, suggesting improved charge transport and minimized leakage pathways at reduced thickness. With further increases in ZnO thickness, R_{sh} decreases due to the increased probability of recombination and defect-assisted leakage. Similarly, the maximum R_{ch} value (~24.38 Ω cm^2) is observed at 10 nm ZnO thickness and subsequently declines as the ZnO layer becomes thicker, reflecting increased resistive losses in the device structure.

Fig. 7(c) describes the relationship b/w the DOS of the BFO layer and the resistive parameters R_s, R_{sh}, and R_{ch}. At a DOS of 1×10^{18} cm^{-3}, R_s exhibits a relatively low value (~8.25 Ω cm^2). However, as the DOS increases to 1×10^{20} cm^{-3}, R_s increases to ~9.76 Ω cm^2 due to enhanced charge carrier recombination associated with a higher density of defect states. The maximum R_{sh} value (~1732 Ω cm^2) is observed at a lower DOS of 1×10^{16} cm^{-3}, indicating suppresses leakage currents and minimal recombination. With increasing DOS, R_{sh} decreases significantly as additional defect states create conductive pathways that facilitate leakage currents and reduced overall device efficiency. The maximum R_{ch} value (~163.23 Ω cm^2) occurs at a DOS of 1×10^{18} cm^{-3}, followed by a slight decline with further increases in DOS, reflecting the growing dominance of recombination-related resistive losses.

Fig. 7(d) illustrates the influence of BFO electron affinity of R_s, R_{sh}, and R_{ch}. The minimum R_s (~0.96 Ω cm^2) is observed at an electron affinity of 2.6 eV, indicating favourable band alignment and efficient charge extraction. As the electron affinity increases, R_s rises to approximately 7.50 Ω cm^2, which can be attributed to reduced carrier extraction efficiency and increased interfacial recombination. The maximum R_{sh} (~1372 Ω cm^2) is achieved at moderate electron affinity values; however, as the electron affinity increases further to 2.8 eV, R_{sh} decreases to ~608 Ω cm^2 due to enhanced recombination and leakage pathways. The highest R_{ch} (~24.38 Ω cm^2) is observed at 2.5 eV, while a slightly lower value (~24.25 Ω cm^2) is obtained near 2.7 eV, reflecting reduced electron and hole extraction efficiency at higher electron affinity values. Overall, these results demonstrate that both structural and electronic parameters critically influence the resistive behaviour and performance of the device.

4. Conclusion

In this study, a physically consistent three-dimensional ZnO/BFO/spiro-OMeTAD perovskite solar cell architecture was investigated using COMSOL Multiphysics to identify the fundamental mechanisms governing device performance. The numerical analysis demonstrates that carrier transport and interface-assisted recombination losses, rather than limitations in bulk

photogeneration, are the dominant factors restricting efficiency in BFO-based devices. This mechanistic insight is supported by the observed sensitivity of device metrics to transport-layer and electronic-structure parameters across the multilayer stack.

The systematic variation of absorber thickness (300–1550 nm), density of states (1×10^{16}–1×10^{20} cm^{-3}), electron affinity (2.5–2.8 eV), and ETL thickness (10–60 nm) reveals that density of states engineering primarily controls open-circuit voltage and fill factor through its influence on recombination kinetics and quasi-Fermi level splitting. For instance, lower DOS values around 1×10^{16} cm^{-3} yielded improved voltage regulation and enabled efficiencies approaching 11.8%, confirming the critical role of defect-mediated recombination. Similarly, optimized band alignment at an electron affinity of approximately 1.8 eV enhanced carrier extraction and suppressed interfacial losses, resulting in a higher V_{oc} exceeding 2.0 V.

The absorber thickness optimization further indicates that a thinner BFO layer around 300 nm is sufficient to achieve efficient charge collection, yielding efficiencies of about 10.8% with $V_{oc} \approx 1.7$ V and $J_{sc} \approx 9.9$ mA cm^{-2}, while avoiding excessive recombination associated with thicker absorbers. In addition, ETL thickness was found to strongly affect series resistance and charge selectivity, with a thickness near 60 nm providing a favorable balance between transport efficiency and recombination suppression, leading to efficiencies above 11.8% and fill factors exceeding 65%.

Overall, these results demonstrate that performance enhancement in ZnO/BFO/spiro-OMeTAD solar cells arises from physically meaningful control of interfacial transport and electronic structure rather than from numerical tuning alone. The coupled electrostatic and carrier-transport framework presented here provides transferable design guidelines for the experimental realization of stable, environmentally friendly, lead-free BFO-derived photovoltaic architectures.

Conflicts of interest

There are no conflicts to declare.

Data availability

The data will be available upon request.

Acknowledgements

The authors acknowledge partial support from University of the Punjab, under Annual Research Grant Program for the fiscal year 2025–26.

References

1 I. Alam, R. Mollick and M. A. Ashraf, Numerical simulation of $Cs_2AgBiBr_6$-based perovskite solar cell with ZnO nanorod and P3HT as the charge transport layers, *Phys. B*, 2021, **618**, 413187.
2 A. Raj, M. Kumar, A. Kumar, K. Singh, S. Sharma, R. C. Singh, M. S. Pawar, M. Z. A. Yahya and A. Anshul, Comparative analysis of 'La'modified BiFeO3-based perovskite solar cell devices for high conversion efficiency, *Ceram. Int.*, 2023, **49**(1), 1317–1327.
3 M. A. Raza, M. M. Aman, L. Kumar, M. A. Al-Khasawneh, M. Faheem and M. A. Ehyaei, Carbon neutrality and economic stability nexus: An integrated renewable energy transition to decarbonize the energy sector, *Energy Rep.*, 2025, **13**, 4586–4608.
4 D. B. Khadka, S. Sagadevan, M. A. U. Islam, S. Kato and T. Soga, Photovoltaic Properties of Bismuth Vanadate/Bismuth Ferrite Heterostructures Prepared by Spin Coating, *Ceram. Int.*, 2025, **51**(1), 449–457.
5 V. N. Muppana, M. Samykano, A. K. Pandey, N. W. Keng, R. K. Rajamony and S. K. Suraparaju, Optimizing Charge Transport and Bandgap Alignment of ETL and HTL in Tin-Based Perovskite Solar Cells via Machine Learning, *Mater. Today Commun.*, 2025, 112874.
6 J. Liang, X. Hu, C. Wang, C. Liang, C. Chen, M. Xiao and G. Fang, Origins and influences of metallic lead in perovskite solar cells, *Joule*, 2022, **6**(4), 816–833.
7 S. Pal, N. V. Sarath, K. S. Priya and P. Murugavel, A review on ferroelectric systems for next generation photovoltaic applications, *J. Phys. D: Appl. Phys.*, 2022, **55**(28), 283001.
8 P. Zhu, D. Wang, Y. Zhang, Z. Liang, J. Li, J. Zeng and B. Xu, Aqueous synthesis of perovskite precursors for highly efficient perovskite solar cells, *Science*, 2024, **383**(6682), 524–531.
9 J. Tan, S. Tong, T. Zhou, J. Lin and Y. Liu, Research and development of modification strategies based on all inorganic perovskite solar cells, *Nano Energy*, 2025, **138**, 110815.
10 A. De Jesús Bautista-Morantes, C. O. Calderón-Carvajal, J. A. Gómez-Cuaspud and E. Vera-López, A new thin-film solar cell prototype based on Na-doped $BiFeO_3$, *Dyna*, 2025, **92**(237), 30–37.
11 F. Pakravesh and M. Izadyar, Theoretical insights into the electronic and optical properties of lithium-based perovskite for solar cell applications, *J. Photochem. Photobiol., A*, 2024, **453**, 115602.
12 A. Sunny, S. Rahman, M. Khatun and S. R. A. Ahmed, Numerical study of high performance HTL-free $CH_3NH_3SnI_3$-based perovskite solar cell by SCAPS-1D, *AIP Adv.*, 2021, **11**(6), 065102.
13 H. Li and S. Liu, Revolutionary SAMs: transforming inverted perovskite solar cells, *J. Mater. Chem. A*, 2024, **12**(17), 9929–9932.
14 P. J. Mokgolo, T. P. Gumede, R. O. Ocaya and T. D. Malevu, Enhancing Perovskite Solar Cells With Rare-Earth Metal Doped Zinc Oxide: A Review of Electron Mobility, Stability, and Photocarrier Recombination, *Int. J. Energy Res.*, 2025, **2025**(1), 4240199.
15 C. Qiu, Y. Wu, J. Song, W. Wang and Z. Li, Efficient planar perovskite solar cells with ZnO electron transport layer, *Coatings*, 2022, **12**(12), 1981.
16 E. Abdelkader, L. Nadjia, B. Naceur and L. Favier Teodorescu, Thermal, structural and optical properties of magnetic

$BiFeO_3$ micron-particles synthesized by coprecipitation method: heterogeneous photocatalysis study under white LED irradiation, *Cerâmica*, 2022, **68**(385), 84–96.

17 H. Renuka, P. K. Enaganti, B. H. Venkataraman, K. Ramaswamy, S. Kundu and S. Goel, Submerged solar energy harvesting using ferroelectric Ti-doped BFO-based heterojunction solar cells, *Int. J. Energy Res.*, 2021, **45**(14), 20400–20412.

18 M. A. Khan, K. Shahbaz, G. M. Mustafa, S. M. Ramay, S. Naseem and S. Atiq, Optimization of magnetoelectric coupling in $BiFeO_3$-$BaTiO_3$-$MnFe_2O_4$ tri-phase composites for ultra-sensitive devices, *J. Alloys Compd.*, 2023, **947**, 169571.

19 A. R. Carrasco-Hernández, A. Reyes-Rojas, G. Rojas-George, A. R. D. la Cruz and H. E. Esparza-Ponce, Evaluation of Physical Properties of Ti-Doped $BiFeO_3$ Thin Films Deposited on Fluorine Tin Oxide and Indium Tin Oxide Substrates, *Materials*, 2025, **18**(10), 2395.

20 D. Jalandhara, S. Kumar, S. Kumar, R. MM, S. V. Sharma and S. Kaushal, $BiFeO_3$ as a Next-Generation Photocatalyst: Bridging Material Design with Environmental Remediation, *ChemPhysChem*, 2025, **26**(10), e202401092.

21 M. U. Salman, M. Bilal, Y. K. Karmani, U. Ali, S. M. Ramay, M. Younis and S. Atiq, Influence of acceptor/donor densities and layer thicknesses on the efficiency of 2D ZnO/BFO/spiro-OMeTAD perovskite solar cells: a COMSOL simulation-based optimization, *J. Mater. Chem. A*, 2025, **13**(20), 15057–15066.

22 G. Kadim, R. Masrour and A. Jabar, Ferroelectric, quantum efficiency and photovoltaic properties in perovskite $BiFeO_3$ thin films: first principle calculations and Monte Carlo study, *Int. J. Energy Res.*, 2021, **45**(7), 9961–9969.

23 L. Zhang, K. Y. Liang, Y. F. Wang, K. Z. Hui, T. Y. Hu, Z. Yang and J. H. Zeng, Elevated Voltage on Sandwiched Semiconductor/Ferroelectric Photovoltaics, *ACS Appl. Energy Mater.*, 2025, **8**(5), 3096–3106.

24 Y. Shen, K. Deng and L. Li, Spiro-OMeTAD-Based Hole Transport Layer Engineering toward Stable Perovskite Solar Cells, *Small Methods*, 2022, **6**(11), 2200757.

25 M. Cheng, C. Zuo, Y. Wu, Z. Li, B. Xu, Y. Hua and L. Ding, Charge-transport layer engineering in perovskite solar cells, *Sci. Bull.*, 2020, **65**(15), 1237–1241.

26 A. Javed, M. F. Nasir, S. Azam and M. A. Amin, Numerical simulation for a suitable electron transport layer of a lead-free $CuInSe_2$ based perovskite solar cell and PV module, *Int. J. Electrochem. Sci.*, 2025, **20**(1), 100893.

27 O. Ceballos-Sanchez, A. Sanchez-Martinez, F. J. Flores-Ruiz, A. M. Huerta-Flores, L. M. Torres-Martínez, R. Ruelas and M. García-Guaderrama, Study of $BiFeO_3$ thin film obtained by a simple chemical method for the heterojunction-type solar cell design, *J. Alloys Compd.*, 2020, **832**, 154923.

28 W. A. Wani, G. Gupta, S. Rath, H. Venkataraman and K. Ramaswamy, Photon upconversion assisted ferroelectric photovoltaics: Device configuration with multifaceted influence in augmenting the photovoltaic response of $BiFeO_3$ thin-film solar cells, *Prog. Photovoltaics Res. Appl.*, 2024, **32**(8), 556–568.

29 A. M. Afzal, Y. Javed, S. Hussain, A. Ali, M. Z. Yaqoob and S. Mumtaz, Enhancement in photovoltaic properties of bismuth ferrite/zinc oxide heterostructure solar cell device with graphene/indium tin oxide hybrid electrodes, *Ceram. Int.*, 2020, **46**(7), 9161–9169.

30 A. Raj, S. Sharma, D. V. Singh, A. Kumar, R. K. Chourasia, J. M. Siqueiros, O. R. Herrera, A. Anshul and M. Kumar, Photovoltaic energy conversion in multiferroic perovskite absorber-based devices via experiment and theoretical calculations, *Phys. B*, 2024, **673**, 415504.

31 N. A. Mahammedi, A. Benameur, H. Gueffaf, B. Merabet, O. M. Ozkendir and S. I. Sato, Investigating a Pb-free nip perovskite solar cell with BFCO absorber using SCAPS-1D, *Optik*, 2024, **302**, 171659.

32 H. Abedini-Ahangarkola and S. Soleimani-Amiri, Design and analysis of high efficiency perovskite solar cells with light trapping nano-textured substrates, *Int. J. Eng.*, 2021, **34**(4), 873–880.

33 Y. F. Makableh, W. Hassan, I. A. Awad and G. Aljaiuossi, Comprehensive Electrical modeling analysis of Heterojunction Perovskite Solar Cells by using different electron transport nanostructured layers, *Superlattices Microstruct.*, 2021, **150**, 106777.

34 S. Elewa, B. Yousif and M. E. A. Abo-Elsoud, Improving efficiency of perovskite solar cell using optimized front surface nanospheres grating, *Appl. Phys. A:Mater. Sci. Process.*, 2021, **127**, 1–14.

35 S. Zandi, P. Saxena and N. E. Gorji, Numerical simulation of heat distribution in RGO-contacted perovskite solar cells using COMSOL, *Sol. Energy*, 2020, **197**, 105–110.

36 M. H. Mohammadi, M. Eskandari and D. Fathi, Morphological investigation and 3D simulation of plasmonic nanostructures to improve the efficiency of perovskite solar cells, *Sci. Rep.*, 2023, **13**(1), 18584.

37 Z. Q. Wang, Z. H. Xiong, W. J. Hu, J. J. Jiang, Z. B. Cheng, Y. M. Xue, L. Peng and J. Lin, Exploration of Double Perovskite Material Space via Machine Learning for Tandem Solar Cells, *Acta Phys. Pol., A*, 2025, **147**(6), 488.

38 G. M. D. Kenfack, F. T. Nya and A. Laref, Organic solar cell efficiency improvement through architecture engineering by integrating carbon nanoring–SCAPS 1D modelling, *Mater. Chem. Phys.*, 2024, **324**, 129713.

39 E. Karimi, S. M. B. Ghorashi and M. Hashemi, Optical and Elecrtical Simulation of $CH_3NH_3PbI_3$-based Perovskite Solar Cells, *Int. J. Opt. Photonics*, 2020, **14**(1), 57–66.

40 S. Bhattarai, M. K. Hossain, J. Madan, R. Pandey, D. P. Samajdar, M. Z. Ansari and M. Amami, Performance improvement of HTL-free perovskite solar cells with the graded approach by numerical simulation, *J. Phys. Chem. Solids*, 2024, **184**, 111691.

41 W. Clarke, M. J. Wolf, A. Walker and G. Richardson, Charge transport modelling of perovskite solar cells accounting for non-Boltzmann statistics in organic and highly-doped transport layers, *J. Phys.: Energy*, 2023, **5**(2), 025007.

42 W. Cheng, Y. Liu, R. Zhou, Y. Yang, C. Wang, Y. Li and L. Chen, Exploring Optoelectronic-Thermal Coupling in Perovskite Solar Cells Utilizing Varied Hole Transport Layers, *Adv. Theory Simul.*, 2024, **7**(3), 2300749.

43 Y. K. Karmani, M. Bilal, M. U. Salman, M. Ameen, M. Luqman, S. M. Ramay and S. Atiq, Correlation between trap-assisted non-radiative recombination losses and thermal agitation in SnS-based solar cell: A state-of-the-art computational analysis, *Mater. Sci. Eng., B*, 2025, **321**, 118484.

44 R. Zhou, Y. Chen, L. Zhou, Y. Yao, Y. Liu, C. Wang and L. Chen, Inhibiting hysteresis and optimizing the performance of perovskite solar cells, *Sol. Energy Mater. Sol. Cells*, 2024, **264**, 112616.

45 A. C. Nkele, I. S. Ike, S. Ezugwu, M. Maaza and F. I. Ezema, An overview of the mathematical modelling of perovskite solar cells towards achieving highly efficient perovskite devices, *Int. J. Energy Res.*, 2021, **45**(2), 1496–1516.

46 U. U. Rehman, K. U. Sahar, E. Hussain and C. M. Wang, Performance optimization of lead-free potassium germanium halide based perovskite solar cells: A numerical study, *Sol. Energy*, 2024, **277**, 112752.

47 L. Huang, Relating band edge DOS occupancy statistics associated excited state electron entropy generation to free energy loss and intrinsic V_{oc} deficit of solar cells, *Phys. Chem. Chem. Phys.*, 2023, **25**(20), 14334–14347.

48 M. M. Mudassar, M. Arshad, M. U. Salman, A. Mahmood, W. Al-Masry, M. Asim and S. Atiq, Significance of the direct relation between the fill factor and hole transport layer thickness in perovskite-based solar cells for green energies, *RSC Adv.*, 2025, **15**(40), 33830–33843.

49 B. M. Soucase, F. Baig, Y. H. Khattak, E. Vega and M. Mollar, Numerical analysis for efficiency limits of experimental perovskite solar cell, *Sol. Energy*, 2022, **235**, 200–208.

50 K. G. Beepat, D. P. Sharma, A. Mahajan, D. Pathak and V. Kumar, Simulation of multijunction solar cell interfaces for enhancement of the power conversion efficiency, *Discover Appl. Sci.*, 2024, **6**(6), 1–19.

51 E. Raza, J. Bhadra, M. Asif, F. Aziz, N. J. Al-Thani and Z. Ahmad, A numerical approach to study the effect of bandgap and electron affinity in HTL-free perovskite solar cells and design of two-terminal silicon/perovskite tandem solar cell, *Mater. Today Commun.*, 2023, **37**, 107383.

52 A. Alsalme, M. F. Altowairqi, A. A. Alhamed and R. A. Khan, Optimization of photovoltaic performance of Pb-free perovskite solar cells via numerical simulation, *Molecules*, 2022, **28**(1), 224.

53 M. U. Salman, M. Mehak, U. Ali, G. M. U. Din, S. M. Ramay, M. Younis and S. Atiq, Direct correlation between open-circuit voltage and quasi-Fermi level splitting in perovskite solar cells: a computational step involving thickness, doping, lifetime, and temperature variations for green solutions, *RSC Adv.*, 2025, **15**(20), 15618–15629.

54 G. M. Mustafa, B. Younas, S. Saba, Z. M. Elqahtani, N. Alwadai and S. Aftab, Numerical simulation to optimize power conversion efficiency of an FTO/GO/$Cs_2AgBiBr_6$/Cu_2O solar cell, *RSC Adv.*, 2024, **14**(27), 18957–18969.

55 W. A. Wani, H. Renuka, S. Kundu, S. Goel, H. Venkataraman and K. Ramaswamy, What ails the photovoltaic performance in single-layered unpoled BFO? –The role of oxygen annealing in improving the photovoltaic efficiency, *Sol. Energy*, 2022, **236**, 822–831.